RESEARCH ARTICLE OPEN ACCESS

A $V_4C_3T_z$//$K_{0.04}MnO_2$ Supercapacitor Cell in a 5 M $LiNO_3$ Electrolyte

Beatriz Mendoza-Sánchez[1] | Enrique Samperio-Niembro[1] | Atharva H. Ladole[1,2] | Liuda Mereacre[1] | Oleksandr Dolotko[1] | Michael Knapp[1] | Camille Douard[3,4] | Thierry Brousse[3,4] | Christopher E. Shuck[5]

[1]Institute for Applied Materials-Energy Storage Systems (IAM-ESS), Karlsruhe Institute of Technology, Eggenstein-Leopoldshafen, Germany | [2]Institute for Energy and Materials Processes-Reactive Fluids, University of Duisburg-Essen, Duisburg, Germany | [3]Nantes Université, CNRS, Institut des Matériaux de Nantes Jean Rouxel, IMN, Nantes, France | [4]Réseau sur le Stockage Electrochimique de l'Energie (RS2E), CNRS FR 3459, Amiens, France | [5]Department of Chemistry and Chemical Biology, Rutgers University, Piscataway, New Jersey, USA

Correspondence: Beatriz Mendoza-Sánchez (beatriz.sanchez.wa@gmail.com)

Received: 19 June 2026 | **Revised:** 19 June 2026 | **Accepted:** 3 July 2026

Keywords: cryptomelane $K_{0.04}MnO_2$ | energy per unit volume | full cell | $V_4C_3T_z$ MXene

ABSTRACT

MXenes are excellent candidates for supercapacitor applications in aqueous electrolytes. Due to their two-dimensionality, which results in a high packing density, MXenes deliver a high energy per unit volume. However, as most MXenes perform in negative electrochemical windows, the challenge in building a full cell device lies on finding a suitable positive electrode that matches the high performance per unit volume of the MXene while being stable in the same electrolyte and enabling a suitable enhancement of the voltage range of the resulting cell. In the case of aqueous electrolytes, activated carbon electrodes have been traditionally used as the positive electrode counterpart of MXenes. However, its low density undermines the performance per unit volume. In this work, we build a full cell using a $V_4C_3T_z$ MXene as negative electrode and cryptomelane-type $K_{0.04}MnO_2$ as positive electrode and evaluate it in a 5 M $LiNO_3$ electrolyte. The full cell performed in a 1.8 V voltage range and showed a superior volumetric energy as compared to a $V_4C_3T_z$//activated carbon cell in a 3 M H_2SO_4 electrolyte at low volumetric power (previously reported by us). The $V_4C_3T_z$//$K_{0.04}MnO_2$ cell also outperformed in volumetric energy other previously reported $Ti_3C_2T_z$//MnO_2 and $Ti_3C_2T_z$//activated carbon cells evaluated in a water-in-salt electrolyte at a medium-to-high power per volume range. An aqueous and neutral electrolyte at standard concentration, such as 5 M $LiNO_3$, brings environmental advantages versus acidic electrolytes and circumvents power performance problems brought in by highly concentrated electrolytes.

1 | Introduction

MXenes have emerged as excellent material for supercapacitor applications [1]. MXenes, $M_{n+1}X_nT_z$, are derived from $M_{n+1}AX_n$ precursors (termed MAX), where $n = 1–4$, M is an early transition metal (Ti, V, Mo, Ta, Nb, etc.), A is an element of the group IIIA or IVA (e.g., Al, Ga, Si, Ge, etc.), X is C and/or N, and T_z describes surface chemical functionalities (–O, –F, and –OH, –Cl groups and others) [2, 3]. In addition, other MXenes combining two M′ and M″ transition metals, $(M'M'')_{n+1}X_nT_z$, have been theoretically predicted and/or experimentally obtained [2, 3]. To date, more than 30 stoichiometric MXenes have been synthesized [3].

MXenes store charge in a variety of acidic and neutral aqueous electrolytes. Particularly, $Ti_3C_2T_z$ performs in aqueous electrolytes consisting of monovalent and multivalent cations H^+, Li^+, Na^+, K^+, Mg^{+2}, Al^{+3} [4, 5]. Other MXenes that perform in aqueous electrolytes include Ti_2CT_z [6], V_2CT_z [7, 8], Mo_2CT_z [9], $Mo_2TiC_2T_z$ [10], and $Nb_4C_3T_z$ [11].

In these aqueous electrolytes, generally, MXenes store charge in negative electrochemical windows (EWs), limited by the hydrogen evolution reaction (HER) at negative potentials and by oxidation of the MXenes at positive potentials. For instance, −0.35 to 0.2 V versus Ag/AgCl for $Ti_3C_2T_z$ in 1 M H_2SO_4 [5] later improved to −0.6 to 0.38 V versus Ag/AgCl in 3 M H_2SO_4 by making use of glassy carbon current collectors with a higher HER overpotential [12]. Equally, V_2CT_z performs in a −0.6 to 0.38 V versus Ag/AgCl EW in 1 M H_2SO_4 [7], Mo_2CT_z performs in a −0.3 to 0.3 V versus Ag/AgCl EW in 1 M H_2SO_4 [9], $Mo_2TiC_2T_z$ performs in a −0.1 to 0.4 V versus Ag/AgCl EW in 1 M H_2SO_4 [10], and $Nb_4C_3T_z$ performs in a −0.9 to 0.1 V versus Ag EW in 1 M H_2SO_4 [11]. Recently, we have reported the performance of $V_4C_3T_z$ in 3 M H_2SO_4 in a −0.35 to 0.4 V versus Ag/AgCl EW [13].

The negative limit of the stable EW can be extended in neutral electrolytes but at the expense of a lower energy density, linked to a lower ionic conductivity, as compared to acidic electrolytes, and energy storage mechanisms limited to double layer capacitance. For instance, $Ti_3C_2T_z$ achieved 245 F g^{-1} in a −0.35 to 0.2 V versus Ag/AgCl EW in 1 M H_2SO_4 [5], but only 85 F g^{-1} in a −0.75 to 0.0 V versus Ag/AgCl EW in K_2SO_4 (concentration not reported) [4]. A clever strategy to enhance EWs without such a drastic decrease of capacitance is the use of acidified electrolytes, which was proposed for $Mo_xV_{4-x}C_3$ [14]. $Mo_{2.7}V_{1.3}C_3T_z$ performed in a −0.4 to 0.45 V versus Ag/AgCl (0.85 V) EW in 1 M H_2SO_4 delivering a capacitance of ca. 270–300 F g^{-1} [14]. The EW was enlarged to −0.55 to 0.4 V versus Ag/AgCl (0.95 V) delivering a capacitance of 150 F g^{-1} in a 1 M Na_2SO_4 electrolyte acidified to a pH = 2.32 [14]. In contrast, when a neutral 1 M Na_2SO_4 was used, the EW was smaller, −0.7 to 0.2 V versus Ag/AgCl (0.9 V) and the capacitance was only 100 F g^{-1}. Since the energy is proportional to the charge stored and the EW (Equation (5)), a larger EW should not be unbalanced with a drastic decrease of capacity to maximize energy.

In view of full cell devices, given the performance of MXenes in negative EWs, the challenge is to find a suitable positive electrode that achieves a performance comparable to MXenes and operates effectively in the same electrolyte. Proposed solutions include the use of activated carbon (AC), or a transition metal oxide (TMO) or another MXene that performs in positive EWs. AC operates in positive EWs, in neutral and acidic electrolytes; however, a drawback is its 3D porous nature resulting in a much lower density than 2D MXenes. This leads to a mismatch in power capability and a low volumetric energy of the resulting full device [13]. Up-to-date studied MXenes perform from −0.7 to 0.3–0.4 V versus Ag/AgCl EWs. Therefore, when used as positive electrodes, a large section of the negative EW is wasted. For instance, in a $Ti_3C_2T_z$//$Mo_{2.7}V_{1.3}C_3T_z$ full cell in 1 M H_2SO_4, $Ti_3C_2T_z$ stores in a −0.7 to −0.1 V versus Ag/AgCl (0.8 V) EW, and the $Mo_{2.7}V_{1.3}C_3T_z$ stores in a −0.4 to 0.45 V versus Ag/AgCl (0.85 V) EW, yet the full device operated in a 0.9–1 V EW, where $Mo_{2.7}V_{1.3}C_3T_z$ operated in a reduced EW of −0.15 to 0.4 V versus Ag/AgCl [14]. TMOs store at positive EW in aqueous electrolytes [1]. The challenge is that they are not stable in acidic electrolytes, where MXenes perform best. Therefore, a full cell using a MXene as negative electrodes and TMOs as positive electrodes must operate in neutral electrolytes.

A suitable TMO candidate for energy storage in neutral aqueous electrolytes is MnO_2. MnO_2 exists in a range of allotropic forms based on MnO_6 octahedra that can form layered or tunneled crystal structures [15]. MnO_2 has shown charge storage in a variety of neutral aqueous electrolytes including $LiNO_3$ (0.5 M, 5 M), Na_2SO_4 (0.1 M), K_2SO_4 (0.5 M, 0.65 M), and $Ca(NO_3)_2$ (0.5 M) [15–18]. The stable EW varies from −0.1–0.0 V to 0.8–1.0 V versus Ag/AgCl EW depending on the electrolyte and the type of allotrope [15–19]. The main energy storage mechanisms include pseudocapacitive surface-based processes that involve the Mn^{+4}/Mn^{+3} redox couple, bulk cation (de-)insertion processes, and surface-based adsorption processes [15]. Energy storage processes and performance are largely dependent on the type of allotrope, i.e., crystal structure and size of the interlayer/tunnel structures relative to the stored cations-solvent species [15]. However, a range of other variables play a crucial role including electronic and ionic conductivity [15], crystallinity [20], surface area, porosity, electrode mass loading, and density [15, 18]. The latter three are strongly correlated with electrode manufacturing procedures [18].

Besides energy storage properties, availability and cost of materials are important variables to consider for implementation in real-world applications. Particularly, cryptomelane $K_nMn^{4+}_{(8-n)}Mn^{3+}{}_nO_{16}$, where n is typically 1.3, offers a balance of suitable energy storage properties and commercial availability at low cost. Cryptomelane is a hollandite type manganese oxide, which has a general $A_nMn_8O_{16}$ formula, where A = Li^+, Na^+, K^+, Ba^{2+} and n is the stoichiometry of the cation A, a tetragonal crystal system, a 2 × 2 tunneled crystal structure that hosts A cations and a I4/m space group. When $n = 0$, we have the so-called α-MnO_2 polymorph, where α makes reference to the hollandite crystal properties. When A = K^+ and $n = 1.3$ we have cryptomelane, and when $0.3 < n < 1.3$ we have a K-deficient cryptomelane. It is suitable to make such distinctions because the literature tends to use indistinctly the terms cryptomelane and α-MnO_2.

Cryptomelane performs in 0.5 M K_2SO_4 electrolyte achieving 125 F g^{-1} with contributions from ion (de-)intercalation and Mn redox processes [15]. This capacitance was superior to other allotropes such as pyrolusite and ramsdellite [15]. Moreover, the electronic conductivity of cryptomelane is 9 mS cm^{-1}, which is superior to that of other allotropes, e.g., 58×10^{-7} S cm^{-1} for birnessite [15]. This brings advantages in charge transfer rates. However, K_2SO_4 is not the the best electrolyte for tunneled MnO_2 polymorphs. Instead, Li^+-based electrolytes lead to a superior energy storage, which is correlated to the ion size in relationship to the tunnel size of the host crystal. It has been reported that α-MnO_2 shows a higher charge storage in Li^+-based electrolytes as compared to Na^+- or K^+-based electrolytes, favoring ion (de-)intercalation [16]. Among Li-ion based electrolytes, $LiNO_3$ is preferred over Li_2SO_4 due to its higher solubility at room temperature (5 vs. 3 M) and concomitant higher ionic conductivity [16].

Herein, we propose cryptomelane as a suitable positive electrode for a $V_4C_3T_z$ MXene negative electrode for the assembly of a $V_4C_3T_z$//$K_{0.04}MnO_2$ full cell considering a neutral aqueous 5 M $LiNO_3$ electrolyte. First, we investigate each electrode in half-cell setups. We investigate the stable EWs and performance of individual electrodes. Subsequently, we assemble a $V_4C_3T_z$//$K_{0.04}MnO_2$ full cell and investigate the suitable cell voltage range, and performance parameters including capacity/

capacitance, rate performance, cycling stability, and energy and power per unit mass and volume.

2 | Experimental Methods

2.1 | Chemicals

Hydrofluoric acid, HF (48 wt%, 27.58 M), hydrochloric acid HCl (37 wt%, 12.17 M), tetrabutylammonium hydroxide, TBAOH (40 wt% in water), LiBr (>99%, Reagent plus), polytetrafluoroethylene (PTFE) dispersion (60 wt% in water) were acquired from Sigma-Aldrich, Germany. Deionized water (DI) of 18.2 M m resistivity was used for synthesis procedures and electrolyte preparation. Commercial cryptomelane-type manganese oxide, under the trade name of α-MnO_2 H.S.A. (high surface area), was acquired from PRINCE International Corporation (Baltimore, MD, USA). Carbon black, nanosized and partially graphitized and with a surface area of 45 $m^2 g^{-1}$, under the trade name of PUREBLACK grade 205-110 carbon, was acquired from SUPERIOR GRAPHITE (Chicago, IL, USA).

2.2 | Synthesis of V_4AlC_3

As reported previously in [13]. Vanadium powder (99.5%, −325 mesh, Alfa Aesar), aluminum powder (99.5%, −325 mesh, Alfa Aesar), and graphite (99%, −325 mesh, Alfa Aesar) were mixed in a 4:1.5:3 atomic ratio (10 g in total). The precursors were balled milled with 5-mm yttria-stabilized zirconia balls (2:1 ball/powder ratio) in plastic jars at 60 rpm for 18 h. The powder mixture was then transferred to alumina crucibles, which were placed into a high temperature tube furnace (Carbolite Gero). Ultrahigh purity Ar (99.999%) gas was continually flown (200 $cm^{-3} min^{-1}$) through the furnace for 1 h prior to heating and during the entire annealing procedure. The furnace was heated to 1500 °C at 3 °C min^{-1}, held for 2 h, then cooled to room temperature at 3 C min^{-1}. The resulting solid block product was milled using a drill press with a TiN-coated milling bit. The powders were then sieved through a 400 mesh sieve, producing powders with a particle size <38 μm. The powders were then washed with HCl 37 wt%; 10 g of powder were added slowly to 20 mL of HCl 37 wt% and stirred overnight. Then, the acid was removed by vacuum-assisted filtration while flushing water until the filtrated liquid had pH = 7. The powders were then dried in vacuum at room temperature.

2.3 | Synthesis of Etched V_4AlC_3

As reported previously in [13]. Prior to etching procedures, particle size selection was performed. Powder of particle size <36 μm was selected (using a 36 μm sieve) for etching processes. For the etching reaction, a 50 mL (4 cm bottom diameter) polytetrafluoroethylene (PTFE) reaction vessel and a 3 cm long magnetic stir bar were used. A HF (12 ML): HCl (12 mL): H_2O (8 mL), for a total of 30 mL, acid mix was carefully placed in the reaction vessel. Then, 1 g of V_4AlC_3 was added in small portions over 20 min while stirring at 50 rpm. The reaction vessel was then closed with the screw top lid giving 70% of the turns necessary to fully close (important to allow gas evolution). The reaction vessel was then immersed in an silicon oil bath maintained at 45 °C with the level of oil up to the height of the reaction mix and magnetic stirring was set to 400 rpm. The reaction was performed for 7 days.

After etching, the reaction mixture was placed in conical centrifuge tubes (150 mL), DI water was added and centrifugation was done at 5000 rpm for 10 min. The acidic supernatant was collected with a pipette and discarded. This step was repeated until the supernatant reached pH 5–6. The etched powder was then further washed and collected by vacuum-assisted filtration, using PVDF membrane filters (0.22 μm pore size). DI water (500 mL) was continuously flushed, then the powders were left to settle and dry over the membrane filter (for 3–5 min) prior to collection.

2.4 | Delamination of Etched V_4AlC_3

As reported previously in [13]. For delamination, the etched powder was added to 10 wt% TBAOH, in a 2:1 mol ratio of TBAOH/V_4C_3, and stirred at 350 rpm, at 35 °C, for 17 h. Afterward, washing steps were carried out to retrieve the TBAOH. The TBAOH intercalated products were placed in conical centrifuge tubes (150 mL), DI water was added and centrifugation was done at 5000 rpm for 10 min. The top 70%–80% volume was pipetted out. This step was repeated until achieving pH 7–8, usually three steps. Then, DI water was added, the product was vigorously shaken by hand for 10 min, followed by centrifugation at 3500 rpm for 30 min. The top 70% volume was pipetted out and constituted the delaminated material. This step was repeated three times to obtain more fractions of delaminated product. The $V_4C_3T_x/H_2O$ suspensions of delaminated material were either immediately processed for film manufacture or stored. Storing of V_4C_3/H_2O suspensions was done in gas-washing bottles bubbling with Ar for 5 min, followed by closing under Ar pressure and stored at 5 °C.

2.5 | $V_4C_3T_z$ Film Manufacture

As reported previously in [13]. Delaminated films were manufactured using vacuum-assisted filtration. A standard glass vacuum filtration system and a Celgard 3501 filter membrane (64 nm pore size) were used. To determine the suspension volume to filter to achieve a determined film thickness, calibration was necessary according to the concentration of the suspension. In general, to reduce concentration and facilitate a faster filtration, as-produced suspensions were purified by a centrifugation step at 5000 rpm for 30 min and collection of the top 70% volume. In general, films were obtained by filtering 20–30 mL of $V_4C_3T_z/H_2O$ purified suspension per film. The film/filter membrane stack was then collected and dried in a *B-585* Büchi glass vacuum oven at room temperature for 5 h. The film was then separated from the membrane filter and the weight and thickness were measured. The films here used had a thickness of 8 μm. Generally, the films were stored in a glove box (<0.1 ppm O_2, <0.1 ppm H_2O).

2.6 | Manganese Oxide Film Manufacture

Commercially available cryptomelane-type manganese oxide (details in Chemicals paragraph) was utilized—X-ray diffraction (XRD) analysis in the Results section showed a $K_{0.04}MnO_2$

stoichiometry. A manganese oxide film was manufactured by combining the manganese oxide powder, carbon black, and PTFE in a 55:35:10 mass ratio in a beaker. Ethanol (2–3 mL) was added to the mix, which was placed in on a hot/magnetic stirring plate for mixing (50 rpm) and heating at 40 °C for 30–60 min. The obtained paste was processed to obtain a film using a home made plastic roller of 150 µm gap. The film was dried at 60 °C overnight. The film was then calendered at 40–50 °C using an electric hot rolling press (4 inch width and variable speed MSK-HRP-01, MIT Co. KJ Group Richmond, CA, USA) to obtain a desired mass loading. For most tests, the mass loading was 2.95 mg cm^{-2} and the thickness of the film was 27 µm. For the cycling tests (Figure S3), the mass loading was 14.5 mg cm^{-2} and the thickness of the film was 179 µm. For half cells, disk electrodes of 3 mm were used. For full cells, the area was adjusted according to the mass required for charge neutrality calculations (Equation (4)).

2.7 | Equipment

Centrifugation was performed using a centrifuge (Thermo Scientific Heraeus Multifuge X1R) equipped with a TX-400 rotor (16.8 cm radius). The relative centrifugal force (RCF), measured in gravity acceleration (g) units, is defined as

$$\mathrm{RCF} = 1.1180^{-5} S^2 \times r \quad (1)$$

where S is the centrifugal rotational speed (rpm) and r is the radius of the rotor (cm). This formula should be used to convert the S cited in this work to RCF.

The mass of the powders was measured using a balance (Sartorius, Germany) with a 0.0001 ± 0.00015 g readability. The mass of electrodes was measured using an ultramicrobalance (Mettler Toledo XPR2U) with a 0.0001 ± 0.00015 mg readability. The thickness of film electrodes was measured with a HEIDENHAIN ND280 length gauge with a 0.0001 mm readability.

2.8 | Materials Characterization Methods

Materials characterization was performed in our previous work [13]. Here, we describe briefly instrumentation. Scanning electron microscopy (SEM) was performed in a ZEISS Merlin (ZEISS, Germany) microscope equipped with a GEMINI II column and using the In Lens detector. Standard and high-resolution high-angle annular dark-field scanning transmission electron microscopy (HAADF–STEM) and electron-energy loss spectroscopy (EELS) were performed using a double C_s corrected FEI Titan^3 60–300 (Linköping, Sweden), operated at 300 kV. EELS was performed using the embedded Gatan imaging filter (GIF) Quantum ERS. Further details on sample preparation and data analysis are given in our previous work [13].

XRD was performed in a STOE STADI P diffractometer with a Mo Kα1 radiation source (λ = 0.7093 Å, 50 kV, 40 mA), a Ge 111 monochromator and a MYTHEN 1D silicon strip detector. The samples were measured using a Debye–Scherrer geometry using glass capillaries. The data for V_4AlC_3 powders and $V_4C_3T_z$ MXenes were acquired from 2θ = 2–92° in 2θ = 0.495° steps and acquisition of 1.98 min/step for a total measuring time of 6 h. Each measurement was done twice to ensure reproducibility. Further details on sample preparation and data analysis are given in our previous work [13]. The data for the manganese oxide powders were acquired from 2θ = 2–72° in 2θ = 0.495° steps and acquisition of 60 s/step for a total measuring time of 3 h.

2.9 | Electrochemical Methods

2.9.1 | *Electrochemical Cells*

Electrochemical tests were performed in 1/4 inch 3-electrode perfluoroalkoxy alkane (PFA) Swagelok cells using 6-mm-diameter glassy carbon rods as current collectors.

Half cells were assembled using disk electrodes of V_4C_3 (3 mm diameter) or $K_{0.04}MnO_2$ (area as required) films as working electrodes, an overcapacitive carbon film as counter electrode (5 mm diameter), an Ag/AgCl as reference electrode and a Celgard 3501 film (6 mm diameter) as separator. A 5 M $LiNO_3$ electrolyte was used, which was degassed with N_2 before electrochemical tests. The manufacture of the overcapacitive carbon electrode has been reported in our previous work [13].

$V_4C_3T_z//K_{0.04}MnO_2$ full cells were assembled using $V_4C_3T_z$ as negative electrode and $K_{0.04}MnO_2$ as positive electrode, a Celgard 3501 film (6 mm diameter) as separator, and 5 M $LiNO_3$ electrolyte.

2.9.2 | *Electrochemical Tests*

Electrochemical tests were performed in a VMP300 (BioLogic) potentiostat using EC-Lab software. Cyclic voltammetry (CV) was the main technique used. The cathodic and anodic charge of CVs $Q^{-/+}$ (C) were calculated using numerical integration according to

$$Q^{-/+} = \int I^{-/+} dt \quad (2)$$

where $I^{-/+}$ are cathodic and anodic current (A) and t (s) is time. Then, charge per unit mass, area, and volume were considered.

The capacitance C (F) was calculated as

$$C^{-/+} = \frac{Q^{-/+}}{(V_2 - V_1)} \quad (3)$$

where V_1 and V_2 (V) are the potential limits of the EW of the CV. Gravimetric and volumetric capacitance were calculated dividing by mass or volume of the electrode (for half cells) or the two electrodes (for full cells).

The Coulombic efficiency (CE) was calculated as $(Q^+/Q^-) \times 100$. For the determination of electrochemically stable windows, chronoamperograms (CAs) were performed at different potentials versus Ag/AgCl, for 30 min for the study of the limits of stability of EWs.

For the $V_4C_3T_z//K_{0.04}MnO_2$ full cell, the mass of the negative and positive electrodes, m^- and m^+, were calculated to ensure charge neutrality according to

$$\widetilde{Q}^{-}m^{-} = \widetilde{Q}^{+}m^{+} = (\widetilde{C}^{-}\Delta V^{-})m^{-} = (\widetilde{C}^{+}\Delta V^{+})m^{+} \quad (4)$$

where $\widetilde{Q}^{-}$ and $\widetilde{Q}^{+}$ are the charge per unit mass, $\widetilde{C}^{-}$ and $\widetilde{C}^{+}$ are the capacitance per unit mass, and ΔV^{-} and ΔV^{+} are the EWs of negative and positive electrodes, respectively. $\widetilde{Q}^{-}$ and $\widetilde{Q}^{+}$ were calculated according to Equation (2) at a defined scan rate.

The energy and power of $V_4C_3T_z//K_{0.04}MnO_2$ full cells were calculated using CV and the following equations

$$E = \frac{1}{2}Q_{\text{cell}}^{-/+}V_{\text{cell}} \quad (5)$$

$$P = \frac{1}{2}Q_{\text{cell}}^{-/+}\nu \quad (6)$$

where $Q_{\text{cell}}^{-/+}$ is the cathodic and anodic charge of the cell, calculated according to Equation (2), V_{cell} is the voltage of the cell, and ν is the scan rate at which the CV test was performed. Gravimetric and volumetric energy densities were calculated dividing by mass or volume of the two electrodes.

3 | Results and Discussion

3.1 | Materials Characterization

The MXene $V_4C_3T_z$ was synthesized according to acid-etching and delamination procedures recently reported by us [13]. The synthesized material consisted of a mix of monolayers and few layers material with a flake size of ≈200 nm to 2.0 μm (Figure 1a). In our previous work, we confirmed the 4:3 atomic structure and the elemental composition including V, C, and surface functional groups T_z = O, F, and Cl, using a range of spectroscopy methods including HRTEM and EELS (Figure 1b,c) [13]. Equally, the presence of V vacancies and pores was identified (Figure 1c), which is a desired property for energy storage applications to promote ion transport across nanosheets [13]. Hence, a $V_{4-x}C_3T_z$ stoichiometry would be more accurate. Nevertheless, for the sake of simplification, we denominate the compound $V_4C_3T_z$ throughout the text. $V_4C_3T_z$ electrodes were obtained by vacuum filtration and used for electrochemical studies (Figure 1d,e).

In our previous work, XRD studies and Rietveld refinement confirmed the crystal structure of V_4AlC_3 corresponding to the P $6_3/m$ m c hexagonal space group with lattice parameters: $a = b = 2.92795$ (±0.00006) Å, $c = 22.7116$ (±0.00051) Å, $\alpha = \beta = 90°$, $\gamma = 120°$ [13]. Further details on Rietveld refinement are given in our previous work [13]. The successful etching and delamination were confirmed by XRD, which was demonstrated by a characteristic shift to lower 2θ angles and broadening of the 002, 004, and 008 reflections (Figure 1f) [13, 21]. As calculated from the 2θ angles of the 002 reflection, the c lattice parameters were: 29.6451 Å (d space of 14.8225 Å) for the etched sample and 30.3364 Å (d space of 15.1682 Å) for the delaminated sample.

The commercial manganese oxide here utilized consists of particles with a particle size distribution range from submicrometer to 8 μm (Figure 2a), integrated by nanorods (Figure 2b). XRD studies revealed the stoichiometry and crystal structure of the compound.

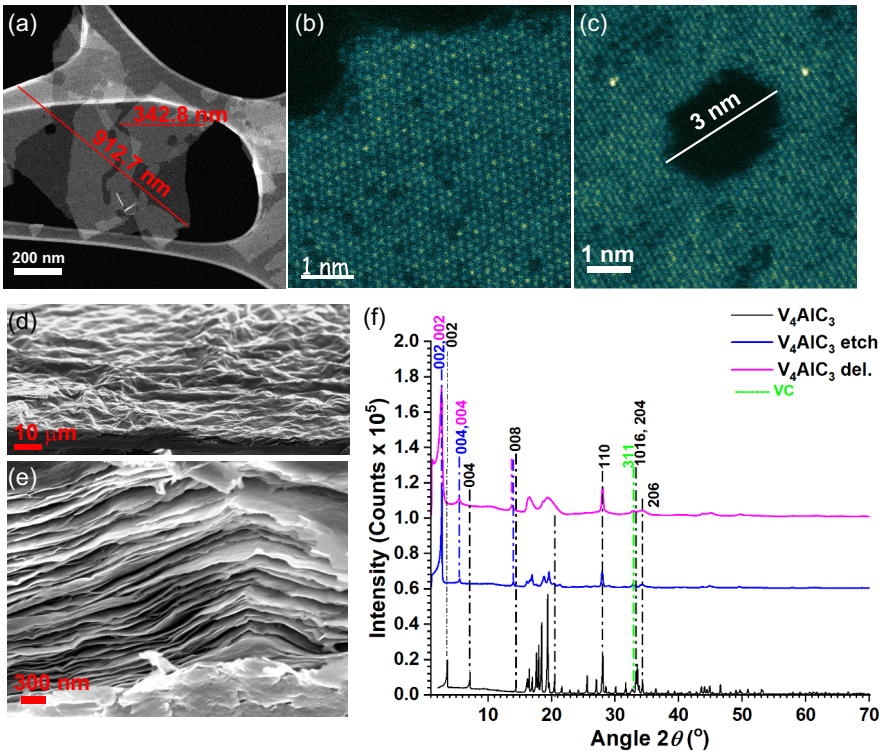

FIGURE 1 | (a) HAADF–STEM image of $V_4C_3T_z$ flakes with lateral size indicated (b,c) HAADF–STEM images of a $V_4C_3T_z$ monolayers showing vacancies and a (c) pore, (d,e) SEM images of a $V_4C_3T_z$ film obtained by vacuum filtration, (f) XRD patterns of V_4AlC_3 and corresponding etched and delaminated samples. Reprinted from [13], Copyright (2024), with permission from Elsevier.

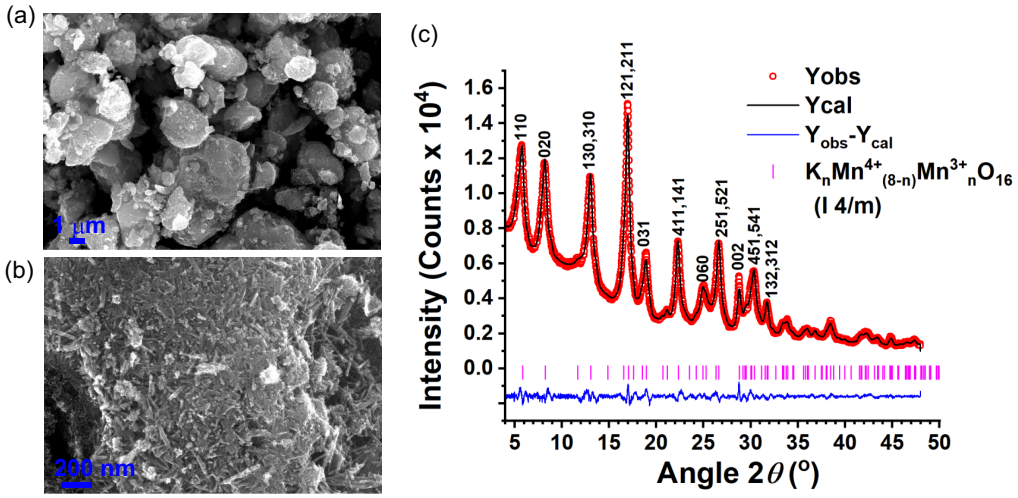

FIGURE 2 | (a,b) SEM images and (c) XRD patterns and calculated model using Rietveld refinement of commercial manganese oxide.

The XRD data were analyzed using the Rietveld refinement method, using the ICDS-59159 reference crystallographic data. Studies confirmed a cryptomelane $K_nMn^{4+}{}_{(8-n)}Mn^{3+}{}_nO_{16}$ compound, which is a member of the hollandite crystal family with 2 × 2 MnO_6 units tunnels [15, 18], tetragonal crystal system, and a symmetry described by the I4/m space group. Considering fixed reported occupancies of O1(0.5), O2(0.5), Mn (0.5), Wyckoff positions and coordinates of K (4e, (0.5, 0.5, 0)), Mn (8h, (x, y, 0)), O1 (8h, (x, y, 0)), O2 (8h, (x, y, 0)), where x, y coordinates were refined, the occupancy of K was determined as 0.0241, which yielded $n = 0.0241 * 16 = 0.3905$ and thus, a $K_{0.39}Mn^{4+}{}_{7.61}Mn^{3+}{}_{0.39}O_{16}$ stoichiometry (= $K_{0.04}MnO_2$). This can be considered a K-deficient cryptomelane—standard cryptomelane has $n = 1.33$ [18]. The lattice parameters were determined as $a = b = 9.8479\ (\pm 0.0227)$ Å and $c = 2.8536\ (\pm 0.0006)$ Å, $\alpha = \beta = \gamma = 90°$, where standard deviations were multiplied by the Bérar factor to correct for local correlations. The profile R factors were $R_p = 2.02$ and $\chi^2 = 2.97$. In our previous work, using nitrogen adsorption isotherms, the Brunauer–Emmett–Teller surface area was determined as 208 $m^2 g^{-1}$ and isotherms were of the type IV describing the mesoporous nature of the powder [18].

3.2 | Electrochemical Studies

The limits of stability of EWs of $V_4C_3T_z$ in 5 M $LiNO_3$ were investigated in a half-cell setup. The OCP was 0.06–0.1 V versus Ag/AgCl. Cyclic voltammograms were performed at 0.5 mV s^{-1} from 0.0 V versus Ag/AgCl toward a negative potentials of −0.7 to −1.1 V versus Ag/AgCl (Figure S1a). CAs were performed at the same potentials for 30 min. Based on the CVs and stable CA currents of 6 μA (−0.27 A g^{-1}) (Figure S1a,b), a negative limit of the EW was set at −0.8 V versus Ag/AgCl. CVs at positive EW were performed from 0.1 V versus Ag/AgCl to 0.4–0.6 V versus Ag/AgCl (Figure S1c,d). We confirmed that $V_4C_3T_z$ does not store charge at positive EWs versus OCP, rather it undergoes oxidation processes at 0.55–0.6 V versus Ag/AgCl (Figure S1c,d). A limit of the stable EW was set at 0.1 V versus Ag/AgCl.

Further CV tests were performed to investigate the charge storage performance of the $V_4C_3T_z$ electrodes (Figure 3). CVs revealed a response typical of a double layer plus pseudocapacitive charge storage mechanism (Figure 3a,b). The electrode had a maximum charge/capacitance of 132.6 C g^{-1}/415 C cm^{-3}/147.4 F g^{-1} (cathodic) at 0.5 mV s^{-1} (Figure 3c,d). The capacity decreased to 31.9% of its initial capacity at 50 mV s^{-1}. This loss of capacity is due to limitations imposed by the typical stacking of 2D nanomaterials that undermines rate performance. The CE was 93.9% at 0.5 mV s^{-1}, increasing to reach 101.8% at 5 mV s^{-1}, and remaining at 101.04% at 100 mV s^{-1}. These CE values larger than 100% at medium scan rates were attributed to limitations of rate performance of the electrode, in which irreversible anodic contributions at the positive limit of the EW made the difference for a slightly larger total anodic charge contribution. At scan rates ≥200 mV s^{-1}, the CE was 99.1%–94.8%. The cycling stability was tested using CV at 10 mV s^{-1} (Figure 3e). The measurement was done in sets of 2000 cycles. The capacity retention was of 65.5% at cycle 10,000. The CE was kept around 102.5%–102.8% over the 10,000 cycles test. The increase of capacitance at 4500 and 6500 cycles is due to a replenishing of electrolyte, upon which a new electrolytic infiltration aided by cycling takes place causing an initial capacity increase.

The CE was improved by reducing the EW to a positive limit of 0.0 V versus Ag/AgCl (Figure S2). In this case, the CE was 99.3%–98.15% between 5 and 100 mV s^{-1}, respectively, keeping below 100% at all scan rates.

Next, the charge storage properties of the $K_{0.04}MnO_2$ electrode in 5 M $LiNO_3$ in a half-cell setup were investigated (Figure 4). This material performs in a 0.0–1.0 V versus Ag/AgCl EW. CVs at 5 mV s^{-1} showed double layer capacitive activity plus cathodic and anodic waves at 0.5 V versus Ag/AgCl, typical of pseudocapacitive activity (Figure 4a). Other redox current peaks due to Li^+ intercalation emerged upon cycling (Figure S3b–e). The electrode showed a charge/capacitance of 82 C g^{-1}/96.1 C cm^{-3}/ 82 F g^{-1} (cathodic) at 5 mV s^{-1} (Figure 4b,c). The charge decreased to 54% at 500 mV s^{-1} (Figure 4b,c). The CE ranged from 100.9% (5 mV s^{-1}) to 104.2% (500 mV s^{-1}) (Figure 4b). This was attributed to small irreversible contributions at the positive limit of the EW due to the oxygen evolution reaction.

The long-term cyclability of the $K_{0.04}MnO_2$ electrode was demonstrated with a CV test at 10 mV s^{-1} for 13,000 cycles, where the

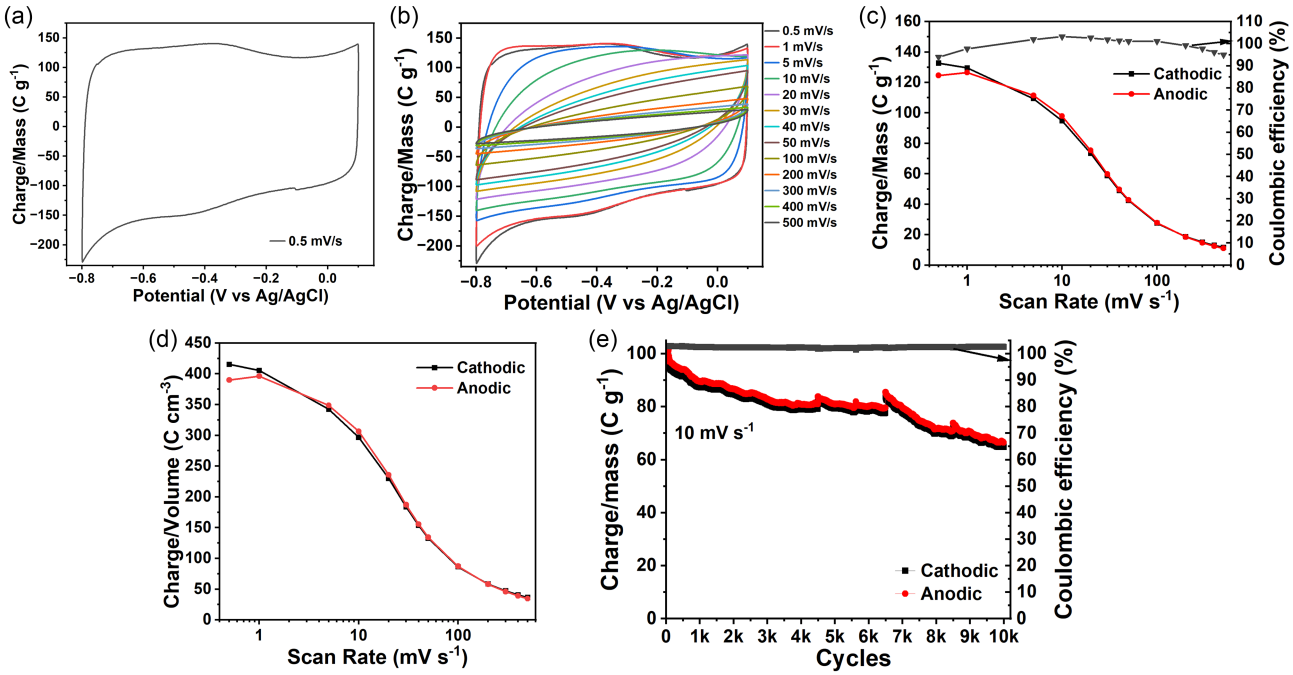

FIGURE 3 | Charge storage of a $V_4C_3T_z$ electrode tested in 5 M $LiNO_3$ and a −0.8 to 0.1 V versus Ag/AgCl EW. (a,b) Cyclic voltammograms at (a) 0.5 mV s^{-1} and (b) 0.5–500 mV s^{-1}, (c,d) charge versus scan rate curves per unit (c) mass and (d) volume; (c) shows also the CE versus scan rate curve, (e) charge per unit mass versus cycles curve, as evaluated using CV at 10 mV s^{-1}.

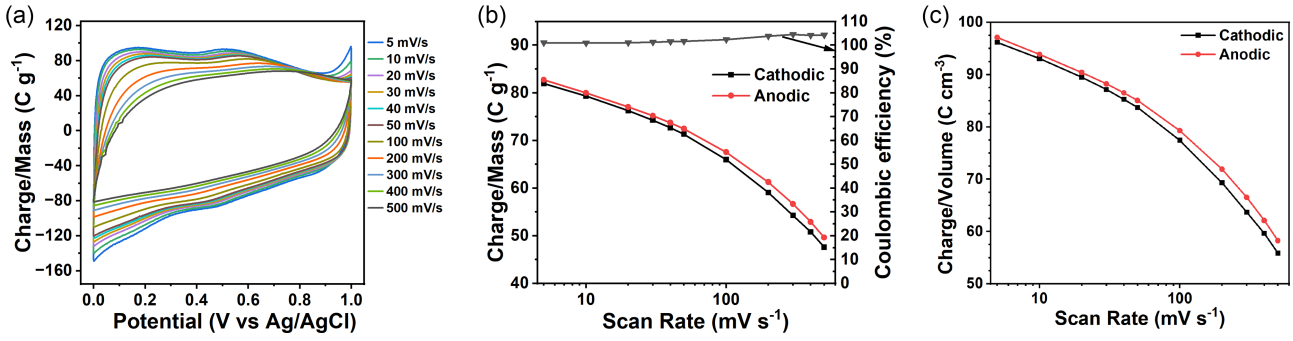

FIGURE 4 | Charge storage of a $K_{0.04}MnO_2$ electrode tested in 5 M $LiNO_3$ and a 0.0 to 1.0 V versus Ag/AgCl EW. (a) Cyclic voltammograms at 5–500 mV s^{-1}, (b,c) charge versus scan rate curves per unit (b) mass and (c) volume; Note: (b) shows also the CE versus scan rate curve.

electrode reached a capacity of 96.1 C g^{-1} (Figure S3a). In this test, other cathodic and anodic redox current peaks due to Li^+ intercalation emerge at cycle 50 and evolve into different and stronger current redox peaks upon cycling (Figure S3b–e). This is due to a continuous wetting of the $K_{0.04}MnO_2$/AC/PTFE electrode upon cycling [18]. Cycling favors an increasingly better penetration of electrolyte into the bulk of the electrode, enabling a better contact between the active material and the electrolyte. This leads also to a continuous increase of charge over cycling (Figure S3a). The oscillations of capacity during this cycling tests are due to day/night temperature variations in the testing room.

Next, a $V_4C_3T_z$//$K_{0.04}MnO_2$ full cell was studied. First, the charge storage of mass-balanced half-cells was studied. A mass balance refers to the calculation of the mass of each electrode in order to ensure charge neutrality of the full cell according to Equation (4). Here, we considered $\Delta V^- = -0.8$ to 0.0 V versus Ag/AgCl and $\Delta V^+ = 0.0$–1 V versus Ag/AgCl for $V_4C_3T_z$ and $K_{0.04}MnO_2$ electrodes, respectively, and charge per unit mass for each electrode, $\tilde{Q}^-$ and $\tilde{Q}^+$, was calculated according to prior independent half-cell tests using a CV at 0.5 mV s^{-1} in the same half-cell EWs. Using the so-calculated electrode masses, half cells were then assembled and tested. A step 1 of the testing was a CV at 10 mV s^{-1} for 30 cycles. This ensured wetting or "activation" of the electrodes. Subsequently, CV tests in a 0.5–500 mV s^{-1} scan rate were performed. CVs of the mass-balanced half cells are shown in Figure S4. At 1 mV s^{-1}, the $V_4C_3T_z$ and $K_{0.04}MnO_2$ electrodes achieved a charge per unit mass of 117.5 C g^{-1}/32.6 mAh g^{-1} and 88.0 C g^{-1}/24.4 mAh g^{-1}, respectively, for a balanced total charge of 0.020 C per electrode. The charge per unit volume was 369.0 C cm^{-3}/102.5 mAh cm^{-3} for the $V_4C_3T_z$ electrode (8 µm thickness) and 103.3 C cm^{-3} /28.7 mAh cm^{-3} for the $K_{0.04}MnO_2$ (27 µm thickness) electrode.

Next, a $V_4C_3T_z$//$K_{0.04}MnO_2$ was assembled. Mass balance for charge neutrality and "activation" procedures using CV at

$10\,mV\,s^{-1}$ for 30 cycles were considered before the main testing. A 1.8 V EW was considered for the full cell (Figure 5). Charge storage was studied using CV at 10–500 $mV\,s^{-1}$ (Figure 5a). A maximum charge storage of $38.7\,C\,g^{-1}/10.7\,mAh\,g^{-1}/21.5\,F\,g^{-1}/\ 45.5\,C\,cm^{-3}$ was achieved at $10\,mV\,s^{-1}$ and had a capacity retention of 38.2% at $500\,mV\,s^{-1}$ (Figure 5b,c). The CE was 101.4% and 103.4% at 10 and 500 $mV\ s^{-1}$, respectively. This slight irreversibility was attributed to anodic processes in the $K_{0.04}MnO_2$ electrode (Figure 4a,b). The cell had a power density of $9.7\,Wh\,kg^{-1}$ at $0.2\,kW\,kg^{-1}$ and $3.7\,Wh\,kg^{-1}$ at $3.7\,KW\,kg^{-1}$ (Figure 5d). The corresponding energy and power performance per unit volume were $11.3\,mWh\,cm^{-3}$ at $0.22\,W\,cm^{-3}$ and $4.3\,mWh\,cm^{-3}$ at $4.3\,W\,cm^{-3}$ (Figure 5e). The rate performance of the cell was studied using galvanostatic cycling with potential limitation (GCPL) from 0.3 to $8\,A\,g^{-1}$ (Figure 5f). At $0.3\,A\,g^{-1}$, it achieved a capacity of $42.3\,C\,g^{-1}$ (discharge) and CE of 100.8%. At $8\,A\,g^{-1}$, it had a $15.3\,C\,g^{-1}$ capacity retaining 37.3% of the capacity at $0.3\,A\,g^{-1}$. The cycling stability was also studied using GCPL at $0.4\,A\,g^{-1}$. The initial capacity was $40\,C\,g^{-1}$ with a CE of 102.5%. The capacity increased continuously over cycling, which is due to the ongoing activation processes on $K_{0.04}MnO_2$ (Figure S3). The CE kept around 102.2%–102.3% (Figure S3). The cycling data were acquired in sets of 2000 cycles. After every new set of data acquisition, the cell underwent a new activation process increasing the capacity during the first cycles.

3.3 | Charge Storage Performance of the $V_4C_3T_z$//$K_{0.04}MnO_2$ Full Cell in Context

We discuss the performance of the $V_4C_3T_z$//$K_{0.04}MnO_2$ cell in the context of other previously reported cells. A $V_4C_3T_z$//AC (AC/carbon black/PTFE in a 75:15:10 wt%) full cell, reported by us, tested in 3 M H_2SO_4 and in a 1.35 V EW, achieved $12.6\,Wh\,kg^{-1}$ at $0.33\,kW\,kg^{-1}$ and $7.3\,Wh\,kg^{-1}$ at $9.74\,kW\,kg^{-1}$ [13] (Figure S5a). This is a superior performance compared to the $V_4C_3T_z$//$K_{0.04}MnO_2$ cell. This is expected as per the superior charge storage in 3 M H_2SO_4, as compared to 5 M $LiNO_3$, of both $V_4C_3T_z$ and AC. However, the advantage of the $V_4C_3T_z$//$K_{0.04}MnO_2$ cell is the volumetric energy. The $V_4C_3T_z$//AC full cell achieved $9.02\,mWh\,cm^{-3}$ at $0.24\,W\,cm^{-3}$ [13]. This is inferior to the performance of the $V_4C_3T_z$//$K_{0.04}MnO_2$ cell ($11.3\,mWh\,cm^{-3}$ at $0.22\,W\,cm^{-3}$) (Figure S5b). However, at a higher power, the performance of the $V_4C_3T_z$//AC was superior with a $5.2\,mWh\,cm^{-3}$ at $6.97\,W\,cm^{-3}$ (Figure S5b).

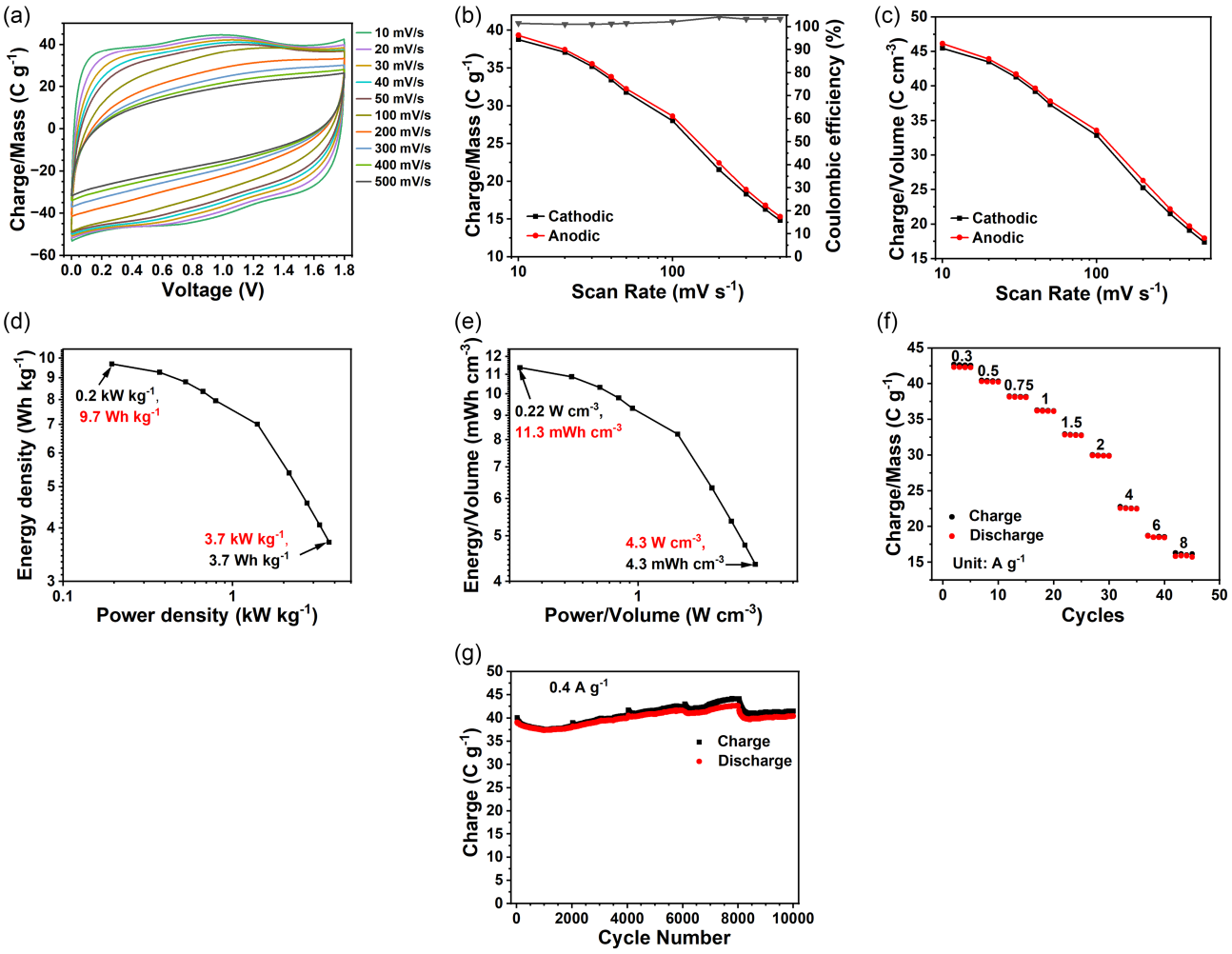

FIGURE 5 | Electrochemical data of a $V_4C_3T_z$//$K_{0.04}MnO_2$ full cell tested in 5 M $LiNO_3$ using CV. (a) CVs at 10–500 $mV\,s^{-1}$, (b,c) charge versus scan rate curves per unit (c) mass and (d) volume, (d,e) corresponding Ragone plots per unit (d) mass and (e) volume, (f) GCPL curves at a range of current rates, (g) charge per unit mass versus cycles curve, as evaluated using a GCPL test at $0.4\,A\,G^{-1}$.

Therefore, the $V_4C_3T_z$//$K_{0.04}MnO_2$ cell brings advantages of performance per unit volume. This is clear when comparing the densities of the $K_{0.04}MnO_2$ (0.78 g cm^{-3}) and the AC (0.47 g cm^{-3}) electrodes. For comparison, the density of the $V_4C_3T_z$ is 2.85 g cm^{-3}. On the other hand, the superior power performance of the $V_4C_3T_z$//AC cell is rooted on the higher ionic conductivity of the acidic 3 M H_2SO_4 electrolyte (732 mS cm^{-1}) as compared to the neutral 5 M $LiNO_3$ electrolyte (170 mS cm^{-1}). Environmental considerations and chemistry stability (as described below) favor the use of neutral rather than acidic electrolytes.

This context brings to light the opportunity for improvement of the performance at high rates of both the $V_4C_3T_z$ and $K_{0.04}MnO_2$. As it is well known, the performance of MXenes is improved by introducing porosity and interlayer spacing [12]. In the case of $K_{0.04}MnO_2$, using a nanosized rather than a microsized material is a good strategy to improve energy density and reduce prior activation periods. Power density could be improved by using other allotropes such as birnessite with a larger interlayer space than cryptomelane (interlayer distance of 7 > 4.6 Å of cryptomelane tunnels) available for rapid ion (de-)intercalation [15] while further engineering of the electrode will increase electronic conductivity.

Another $Ti_3C_2T_z$//$Mo_{2.7}V_{1.3}C_3T_z$ full cell has been reported using 1 M H_2SO_4 and other electrolytes such as acidified 1 M Na_2SO_4 (pH = 2.32) [14]. In the 1 M H_2SO_4 electrolyte, despite a −0.7 to −0.1 V versus Ag/AgCl (0.8 V) EW for $Ti_3C_2T_z$ and −0.4 to 0.45 V versus Ag/AgCl (0.85 V) EW for $Mo_{2.7}V_{1.3}C_3T_z$, the full cell performed in a 0.9–1 V EW, where $Mo_{2.7}V_{1.3}C_3T_z$ operated in a reduced EW of −0.15 to 0.4 V versus Ag/AgCl. This means that a large part of the useful EW of $Mo_{2.7}V_{1.3}C_3T_z$ is wasted. This highlight the advantage of materials such as the $K_{0.04}MnO_2$ here used, with a truly positive EW from 0 to 1 V versus Ag/AgCl. The EW of the $Ti_3C_2T_z$//$Mo_{2.7}V_{1.3}C_3T_z$ full cell in the acidified 1 M Na_2SO_4 was extended to 1.3 V. The reported volumetric capacitance/charge per unit volume at 5 mV s^{-1} are 175 F cm^{-3}/157.5 C cm^{-3} in the 1 M H_2SO_4 electrolyte and 45 F cm^{-3}/58.5 C cm^{-3} in the acidified 1 M Na_2SO_4 [14]. As expected, the volumetric charge achieved by this full cell in the 1 M H_2SO_4 electrolyte is larger than our $V_4C_3T_z$//$K_{0.04}MnO_2$ cell in 5 M $LiNO_3$ (45.5 C cm^{-3} at 10 mV s^{-1}), whose performance is more at the level of the $Ti_3C_2T_z$//$Mo_{2.7}V_{1.3}C_3T_z$ cell in the acidified 1 M Na_2SO_4 electrolyte. However, the downside of the $Ti_3C_2T_z$//$Mo_{2.7}V_{1.3}C_3T_z$ cell in the 1 M H_2SO_4 electrolyte is a poorer cycling stability with a decrease of capacitance to 82% after 7000 cycles, whereas the cell in the acidified 1 M Na_2SO_4 electrolyte performed up to 10,000 cycles with a better capacitance retention of 94% [14]. The degradation upon cycling in the 1 M H_2SO_4 electrolyte was attributed to vanadium leaching in $Mo_{2.7}V_{1.3}C_3T_z$ [14]. This supports our views on limitations of acidic electrolytes and needs to move toward the use of neutral electrolytes, especially when chemistry is not compatible with acidic environments. On the other hand, despite that this is a MXene–MXene full cell, the volumetric charge does not significantly differ from our cell that uses a much thicker and lower density $K_{0.04}MnO_2$ electrode.

Other full cells using water-in-salt electrolytes have been previously reported, where the main target is to enhance energy density by enlarging the operating EW. A $Ti_3C_2T_z$//MnO_2 cell in 21 m KAcO (potassium acetate) and a 2.1 V EW reports 5.8 mWh cm^{-3} at 1.8 W cm^{-3} [22]. This is an inferior performance, as compared to 8.2 mWh cm^{-3} at 1.6 W cm^{-3} of the $V_4C_3T_z$//$K_{0.04}MnO_2$ cell in 5 M $LiNO_3$ here reported (Figure S5b). However, at a lower volumetric power, this $Ti_3C_2T_z$//MnO_2 cell achieved a higher volumetric energy of 16.8 mWh cm^{-3} at 0.13 W cm^{-3} (>11.3 mWh cm^{-3} at 0.22 W cm^{-3} for the $V_4C_3T_z$//$K_{0.04}MnO_2$ cell) (Figure S5b). Another AC//AC cell in a 21 m KAcO electrolyte and a 2.1 V EW had 12.7 mWh cm^{-3} at 0.11 W cm^{-3} and 4.5 mWh cm^{-3} at 1.7 W cm^{-3} [22]. The later performance is inferior to the $V_4C_3T_z$//$K_{0.04}MnO_2$ cell here presented (Figure S5b).

A Table that compares the performance of our full cell with other previously reported full cells is provided in an independent file (excel format) as Supporting Information.

In summary, the $V_4C_3T_z$//$K_{0.04}MnO_2$ cell in 5 M $LiNO_3$ brings a superior volumetric energy at low volumetric power as compared to a $V_4C_3T_z$//AC in 3 M H_2SO_4 cell. However, at higher power, the advantages of an acidic electrolyte show up. On the other hand, some chemistries, such as $Mo_{2.7}V_{1.3}C_3T_z$, are not compatible with highly acidic electrolytes. Cells using water-in-salt electrolyte with a larger EW achieve a superior volumetric energy at low volumetric power than the $V_4C_3T_z$//$K_{0.04}MnO_2$ cell in 5 M $LiNO_3$ and the $V_4C_3T_z$//AC in 3 M H_2SO_4 cell. However, most full cells using water-in-salt electrolytes have an inferior performance at high volumetric power as compared to cells using aqueous electrolytes at a standard concentration. As it stands, there is no perfect system offering a high energy density at high power density. Opportunities for improvement remain for all systems, which should be tailored for targeted applications while considering cost and environmental aspects.

4 | Conclusions

The performance of a $V_4C_3T_z$//$K_{0.04}MnO_2$ full cell in 5 M $LiNO_3$ was investigated. The cell performs in a 1.8 V voltage window delivering 38.7 C g^{-1}/10.7 mAh g^{-1}/21.5 F g^{-1}/45.5 C cm^{-3} and 9.7 Wh kg^{-1} at 0.2 kW kg^{-1}/11.3 mWh cm^{-3} at 0.22 W cm^{-3}. The cells bring advantages of superior volumetric energy as compared to cells using AC as positive electrodes and constitute a more environmentally friendly alternative using a neutral rather than acidic aqueous electrolyte.

Author Contributions

Beatriz Mendoza-Sánchez: conceptualization, methodology, software, validation, formal analysis, investigation, resources, data curation, writing – original draft, writing – review & editing, visualization, supervision, project administration, resources, funding acquisition. **Enrique Samperio-Niembro**: investigation. **Atharva H. Ladole**: investigation. **Liuda Mereacre**: investigation. **Oleksander Dolotko**: investigation. **Michael Knapp**: resources, funding acquisition. **Camille Douard**: investigation. **Thierry Brousse**: formal analysis, writing – review & editing. **Christopher E. Shuck**: investigation, writing – review & editing.

Acknowledgments

B.M.-S. acknowledges the Helmholtz Association for a Helmholtz ERC Recognition Award (ERC-RA-0028). C.D. and T.B. acknowledge Labex STORE-EX (ANR-10-LABX-7601) for financial support. Yury Gogotsi (Drexel University) is acknowledged for his kind gesture providing MAX

materials. This work contributes to the research performed at the Centre for Electrochemical Energy Storage Ulm-Karlsruhe (CELEST).

Open Access funding enabled and organized by Projekt DEAL.

Funding

This work was supported by the Helmholtz-Gemeinschaft (ERC-RA-0028) and Agence Nationale de la Recherche (ANR-10-LABX-76-01).

Conflicts of Interest

The authors declare no conflicts of interest.

Data Availability Statement

The data that support the findings of this work are available upon request to the corresponding author.

References

1. B. Mendoza-Sánchez and Y. Gogotsi, "Synthesis of Two-Dimensional Materials for Capacitive Energy Storage," *Advanced Materials* 28, no. 29 (2016): 6104–6135, https://doi.org/10.1002/adma.201506133.

2. B. Anasori, M. R. Lukatskaya, and Y. Gogotsi, "2D Metal Carbides and Nitrides (MXenes) for Energy Storage," *Nature Reviews Materials* 2, no. 2 (2017): 16098, https://doi.org/10.1038/natrevmats.2016.98.

3. A. VahidMohammadi, J. Rosen, and Y. Gogotsi, "The World of Two-Dimensional Carbides and Nitrides (MXenes)," *Science* 372, no. 6547 (2021): eabf1581, https://www.science.org/doi/abs/10.1126/science.abf1581.

4. M. R. Lukatskaya, O. Mashtalir, C. E. Ren, et al., "Cation Intercalation and High Volumetric Capacitance of Two-Dimensional Titanium Carbide," *Science* 341, no. 6153 (2013): 1502–1505, http://www.ncbi.nlm.nih.gov/pubmed/24072919.

5. M. Ghidiu, M. R. Lukatskaya, M.-Q. Zhao, Y. Gogotsi, and M. W. Barsoum, "Conductive Two-Dimensional Titanium Carbide Clay with High Volumetric Capacitance," *Nature* 516, no. 7529 (2014): 78–81, https://doi.org/10.1038/nature13970.

6. Y. Yoon, M. Lee, S. K. Kim, et al., "A Strategy for Synthesis of Carbon Nitride Induced Chemically Doped 2D MXene for High-Performance Supercapacitor Electrodes," *Advanced Energy Materials* 8, no. 15 (2018): 1703173, https://doi.org/10.1002/aenm.201703173.

7. Q. Shan, X. Mu, M. Alhabeb, et al., "Two-Dimensional Vanadium Carbide (V_2C) MXene as Electrode for Supercapacitors with Aqueous Electrolytes," *Electrochemistry Communications* 96 (2018): 103–107, https://doi.org/10.1016/j.elecom.2018.10.012.

8. A. VahidMohammadi, M. Mojtabavi, N. M. Caffrey, M. Wanunu, and M. Beidaghi, "Assembling 2D MXenes into Highly Stable Pseudocapacitive Electrodes with High Power and Energy Densities," *Advanced Materials* 31, no. 8 (2019): 1806931, https://doi.org/10.1002/adma.201806931.

9. J. Halim, S. Kota, M. R. Lukatskaya, et al., "Synthesis and Characterization of 2D Molybdenum Carbide (MXene)," *Advanced Functional Materials* 26, no. 18 (2016): 3118–3127, https://doi.org/10.1002/adfm.201505328.

10. B. Anasori, Y. Xie, M. Beidaghi, et al., "Two-Dimensional, Ordered, Double Transition Metals Carbides (MXenes)," *ACS Nano* 9, no. 10 (2015): 9507–9516, https://doi.org/10.1021/acsnano.5b03591.

11. S. Zhao, C. Chen, X. Zhao, et al., "Flexible $Nb_4C_3T_x$ Film with Large Interlayer Spacing for High-Performance Supercapacitors," *Advanced Functional Materials* 30, no. 47 (2020): 2000815, https://doi.org/10.1002/adfm.202000815.

12. M. R. Lukatskaya, S. Kota, Z. Lin, et al., "Ultra-High-Rate Pseudocapacitive Energy Storage in Two-Dimensional Transition Metal Carbides," *Nature Energy* 2, no. 8 (2017): 17105, https://doi.org/10.1038/nenergy.2017.105.

13. B. Mendoza-Sánchez, A. H. Ladole, E. Samperio-Niembro, et al., "On the Atomic Structure of Monolayer $V_4C_3T_z$ and the Study of Charge Storage Processes in an Acidic Electrolyte Using SPEIS and in-Situ X-Ray Absorption Spectroscopy," *Energy Storage Materials* 71 (2024): 103566, https://doi.org/10.1016/j.ensm.2024.103566.

14. D. Pinto, B. Anasori, H. Avireddy, et al., "Synthesis and Electrochemical Properties of 2D Molybdenum Vanadium Carbides Solid Solution MXenes," *Journal of Materials Chemistry A* 8, no. 18 (2020): 8957–8968, https://doi.org/10.1039/D0TA01798A.

15. O. Ghodbane, J.-L. Pascal, and F. Favier, "Microstructural Effects on Charge-Storage Properties in MnO_2-Based Electrochemical Supercapacitors," *ACS Applied Materials & Interfaces* 1, no. 5 (2009): 1130–1139, https://doi.org/10.1021/am900094e.

16. H. A. Mosqueda, O. Crosnier, L. Athouël, et al., "Electrolytes for Hybrid Carbon-MnO_2 Electrochemical Capacitors," *Electrochimica Acta* 55, no. 25 (2010): 7479–7483, https://doi.org/10.1016/j.electacta.2010.01.022.

17. A. Gambou-Bosca and D. Bélanger, "Electrochemical Characterization of MnO_2-Based Composite in the Presence of Salt-in-Water and Water-in-Salt Electrolytes as Electrode for Electrochemical Capacitors," *Journal of Power Sources* 326 (2016): 595–603, https://doi.org/10.1016/j.jpowsour.2016.04.088.

18. C. Douard, L. Athouël, D. Brown, et al., "Electrode Design for MnO_2-Based Aqueous Electrochemical Capacitors: Influence of Porosity and Mass Loading," *Materials* 14, no. 11 (2021): 2990, https://www.mdpi.com/1996-1944/14/11/2990.

19. C.-C. Hu and T.-W. Tsou, "Ideal Capacitive Behavior of Hydrous Manganese Oxide Prepared by Anodic Deposition," *Electrochemistry Communications* 4, no. 2 (2002): 105–109, https://doi.org/10.1016/S1388-2481(01)00285-5, https://www.sciencedirect.com/science/article/pii/S1388248101002855.

20. T. Brousse, M. Toupin, R. Dugas, L. Athouël, O. Crosnier, and D. Bélanger, "Crystalline MnO_2 as Possible Alternatives to Amorphous Compounds in Electrochemical Supercapacitors," *Journal of the Electrochemical Society* 153, no. 12 (2006): A2171, https://doi.org/10.1149/1.2352197.

21. B. Mendoza-Sánchez, E. Samperio-Niembro, O. Dolotko, et al., "Systematic Study of the Multiple Variables Involved in V_2AlC Acid-Based Etching Processes, a Key Step in MXene Synthesis," *ACS Applied Materials & Interfaces* 15, no. 23 (2023): 28332–28348, https://doi.org/10.1021/acsami.3c01671.

22. H. Avireddy, B. W. Byles, D. Pinto, et al., "Stable High-Voltage Aqueous Pseudocapacitive Energy Storage Device with Slow Self-Discharge," *Nano Energy* 64 (2019): 103961, https://www.sciencedirect.com/science/article/pii/S2211285519306688.

Supporting Information

Additional supporting information can be found online in the Supporting Information section.